Evaporative Drying from Hydrophilic or Hydrophobic Homogeneous Porous Columns: Consequences of Wettability, Porous Structure and Hydraulic Connectivity

Partha Pratim Chakraborty, Molly Ross, Hitesh Bindra, Melanie M. Derby
Department of Mechanical and Nuclear Engineering, Kansas State University, Manhattan, Kansas, 66506, USA

Corresponding Author: Melanie M. Derby, derbym@ksu.edu
ORCID ID: Partha Pratim Chakraborty (0000-0002-6409-6641)
Molly Ross (0000-0002-7489-2238)
Hitesh Bindra (0000-0001-8928-1328)
Melanie M. Derby (0000-0001-6596-9160)

Abstract

Evaporative drying from porous media is influenced by wettability and porous structures; altering these parameters impacts capillary effects and hydraulic connectivity, thereby achieving slower or faster evaporation. In this study, water was evaporated from a homogeneous porous column created with ~1165 glass (i.e., hydrophilic) or Teflon (i.e., hydrophobic) 2.38-mm-diameter spheres with an applied heat flux of 1000 W/m^2 supplied via a solar simulator; each experiment was replicated five times and lasted seven days. This study investigates the combination of altered wettability on evaporation with an imposed heat flux to drive evaporation, while deploying X-ray imaging to measure evaporation fronts. Initial evaporation rates were faster (i.e., ~1.5 times) in glass than in Teflon. Traditionally, evaporation from porous media is categorized into three periods: constant rate, subsequent falling rate and slower rate period. Due to homogeneous porous structure and similar characteristic pore size (i.e., 0.453 mm), capillary effects were limited, resulting in an insignificant constant evaporation rate period. A sharp decrease in evaporation rate (i.e., falling rate period) was observed, followed by the slower rate period characterized by Fick's law of diffusion. Teflon samples entered the slower rate period after 70 hours compared to 90 hours in glass, and combined with X-ray visualization, implying a lower rate of liquid island formation in the Teflon samples than the glass samples. The evaporative drying front, visualized by X-rays, propagated faster in glass with a final depth (after seven days) of ~30 mm, compared to ~24 mm in Teflon. Permeability was modeled based on the geometry [e.g., 3.163E-9 m^2 (Revil, Glover, Pezard, and Zamora model), 3.287E-9 m^2 (Critical Path Analysis)] and experimentally measured for both glass (9.5E-10 m^2) and Teflon (8.9E-10 m^2) samples. Rayleigh numbers (*Ra*=2380) and Nusselt (*Nu*=4.1) numbers were calculated for quantifying natural evaporation of water from fully saturated porous media, Bond (*Bo*=193E-3) and Capillary (*Ca*=6.203E-8) numbers were calculated and compared with previous studies.

Keywords*: Homogeneous, Hydraulic connectivity, Liquid island, Wettability, Porous media*

Article Highlights

- Drying of water from porous media consisting of 1165 glass (water-loving) and Teflon (water-fearing) spheres was analyzed
- Drying was faster in glass than in Teflon sample due to formation of water films which created a continuous liquid channel

- Due to similar-sized spheres and large pore size, constant drying rate was insignificant in both samples

Declarations

Funding
This research was supported by NSF grants #1651451 and #1828571, and this material is based upon work supported by the Department of Energy under Award DE-NE008690.

Conflicts of interest
The authors do not have any conflict of interest.

Availability of data and material
Data are provided in an electronic supplement.

Code availability
Not applicable.

Nomenclature

a	Pixel value from the X-ray detector	RH	Relative humidity [%]
A	Cross sectional area [m^2]	r_{eff}	Effective pore radius [m or mm]
b	Log transform of the pixel value	r_1, r_2	Pore sizes [mm]
Bo	Bond Number [-]	r_{avg}	Average bead radius [mm]
c	Pore shape factor	S	Transient saturation [%]
C	Constant co-efficient	Sh	Sherwood Number [-]
Ca	Capillary number [-]	t	Material thickness
C_{sat}	Saturated water-vapor density at surface [kg/m^3]	T	Temperature [$°C$]
C_∞	Water-vapor density at ambient [kg/m^3]	V	Volume [m^3]
d	Diameter [m or mm]	**Greek Symbols**	
d_c	Critical diameter [mm]		
D	Mass diffusivity [m^2/s]	α	Thermal diffusivity [m^2/s]
E	Rate of evaporation [mm/day]	Λ	Characteristic pore radius [m or mm]
F	Formation factor	β	Packing angle [°]
g	Acceleration due to gravity [m/s^2]	η	Attenuation coefficient
H	Height of beaker [mm]	θ	Volumetric content [m^3/m^3]
		θ_{tilt}	Tilt angle
h	Convective heat transfer coefficient [W/m^2-K]	μ	Dynamic viscosity [N-s/m^2]
h_b	Pressure head [m]	ν	Kinematic viscosity [m^2/s]
h_m	Mass transfer coefficient [m/s]	ρ	Density [kg/m^3]
I	Attenuated X-ray intensity	σ	Interfacial tension [N/m]
I_0	X-ray beam intensity	ϕ	Porosity [%]
J	Diffusive flux [kg/m^2-s]		
k	Permeability [m^2]	**Subscripts/Superscripts**	
k_a	Thermal conductivity of air [W/m-k]	w	water

K	Saturated hydraulic conductivity [m/s]	L	liquid
L_c	Characteristic length for capillarity [mm]	sat	saturated
L^*	Characteristic length, A/P [mm]	c	critical
L_D	Drying front depth [mm]	i	initial
m	Cementation factor	$frac$	Fractional
Nu	Nusselt number [-]	∞	ambient
n	Fitting parameter		
P	Perimeter [mm]		
Q	Flow rate [m^3/s]		
Ra	Rayleigh number [-]		

1. Introduction

Evaporation from porous media has multiple applications, such as evaporative cooling at the micro-scale (Khrustalev and Faghri, 1995, Kobayashi, et al., 1996) and macro-scale (Mantelli, 2016, Saneinejad, et al., 2012), heat pipes (Hanlon and Ma, 2003, Li, et al., 2013), fuel cells (Chapuis, et al., 2008, Médici and Allen, 2013), food drying (Onwude, et al., 2021, Purlis, 2019), and soil-water dynamics (Or, et al., 2013, Shokri, et al., 2010). Based on the application, faster or slower evaporation rates may be desirable and can be initiated by altering the wettability (Shokri, et al., 2008, Shokri, et al., 2010) and porous structure (Cejas, et al., 2016, Nachshon, et al., 2011). Previous research studied evaporation from porous media based on stages of evaporation (Aboufoul, et al., 2019, Lehmann, et al., 2008, Or, et al., 2013, Shokri, et al., 2009, Shokri, et al., 2010), porosity analysis (Cejas, et al., 2016, Lehmann, et al., 2008, Nachshon, et al., 2011, Prommas, 2011, Thiery, et al., 2017), capillary effects (Lehmann, et al., 2008, Prime, et al., 2015, Shokri, et al., 2009), formation of liquid bridges/island (Chakraborty and Derby, 2020, Chakraborty, et al., 2018, Chen, et al., 2017, Chen, et al., 2018, De Vries, 1958, Kohout, et al., 2006, Philip and De Vries, 1957, Scheel, et al., 2008, Shokri, et al., 2009, Shokri, et al., 2008, Shokri and Or, 2011, Yiotis, et al., 2004), and effects of wettability (Chapuis and Prat, 2007, Shahidzadeh-Bonn, et al., 2004, Shokri, et al., 2008, Shokri, et al., 2009, Shokri, et al., 2010). In most cases, porous media consisted of heterogeneous (Prommas, 2011) particles, but some studies were done on homogeneous (Thiery, et al., 2017) media to distinguish between two combinations.

Typically, evaporation stages from porous media are classified into three distinct groups: constant-rate, falling-rate, and slow-rate period (Hillel, 1998, Lehmann, et al., 2008, Shokri, et al., 2008, Shokri, et al., 2009, Shokri, et al., 2009, Shokri, et al., 2010, Shokri, et al., 2008). In the

constant rate period, the porous media remains saturated, and water is evaporated from the surface by means of natural or forced convection maintaining a constant rate for a certain time period (Shokri, et al., 2009) (Lehmann, et al., 2008) and it continues until the water can move to the top surface by action of capillary force. The depth of drying front at the end of constant rate is marked as the characteristic length, which is defined as the maximum potential hydraulically connected region from the evaporative front to the top surface and constant rate continues until the drying front depth is less than the characteristic length (Lehmann, et al., 2008). The constant rate period is followed by a sharp decrease in evaporation rate called as falling rate period (Hillel, 1998) and, subsequently, a diffusion-controlled (Shokri, et al., 2009, Shokri and Or, 2011) slower rate period starts with negligible evaporation.

Porous structure and pore size distribution also play a vital role in soil-water dynamics and capillary action. Porous structures (e.g., 0.1-0.5 mm grain size) can induce capillary action which can elongate the constant evaporation period (Lehmann, et al., 2008). Certain differences were observed in samples with 150-300 μm and 1-2 mm particles; in the 150-300 μm sample, the characteristic length was greater which resulted in longer duration of constant rate period (~ seven days) (Nachshon, et al., 2011). In a study of evaporation with combinations of 0.4-mm and 0.15-mm glass spheres, smaller spheres on the top of larger accelerated more evaporative mass loss at a constant rate than the other three combinations (e.g., 0.4-mm spheres on top of 0.15-mm spheres), 0.4-mm spheres, and 0.15-mm spheres) (Prommas, 2011). In a series of evaporation experiments from porous media consisted of spheres ranging from 6 nm to 45 μm, the constant rate period was more prevalent in smaller size porous matrices (Thiery, et al., 2017). Heterogeneous media was observed to create more capillary action and subsequent constant rate evaporation than homogenous media due to higher capillary pressure difference between different sized pores (Lehmann, et al., 2008, Nachshon, et al., 2011).

Proper hydraulic connection between saturated and unsaturated or semi-saturated portions of the porous media can accelerate the evaporation process, and it depends on the formation of liquid islands which is influenced by porous structure and wettability. In an observation of evaporation of water from a heterogeneous sand column (260-mm-height, 75-mm-width, and 11-mm-thickness), liquid clusters among adjacent particles were noticed throughout the porous media which supplied water to the evaporative surface (Shokri, et al., 2009, Shokri, et al., 2008, Shokri and Or, 2011). In a cylindrical porous media, liquid islands were formed between adjacent cylinders and subsequently

created a hydraulic effect towards the evaporative front which was termed a secondary capillary effect (Chen, et al., 2017, Chen, et al., 2018). The influence of liquid films in formation of macroscopic liquid islands was analytically formulated while drying from 2D porous network and noticeable significance was found in maintaining hydraulic connection (Yiotis, et al., 2004). Pore size and porous configuration also affect the formation of liquid films. In three different combinations of 1-mm-diameter glass spheres with straight, loose and closed packing, thin liquid films were formed more in closed packing while straight and loose packing held more water due to inability of forming enough liquid islands to maintain hydraulic connection during evaporation (Cejas, et al., 2016).

Evaporation rates and formation of liquid islands depend on the wettability of porous media and based on wettability, materials can be divided into hydrophilic (i.e., contact angle < 90°) and hydrophobic (i.e., contact angle > 90°). Inclusion of hydrophobicity can decrease the evaporation rate by 50-65% (Bachmann, et al., 2001); the study included isothermal conditions (i.e., 20 oC) and non-isothermal conditions (i.e., bottom boundary temperature at 55 ^{o}C, and top boundary temperature at 21 ^{o}C). In a study of evaporation of water from heterogeneous, 255-mm-long sand columns, the lowest evaporation rate was found in sand columns of 25-mm hydrophobic sand on the top of hydrophilic one and 7-mm hydrophobic sand layer placed 18-mm below the hydrophilic surface (Shokri, et al., 2008, Shokri, et al., 2010); these experiments were conducted at 25 ^{o}C and 45% RH, with no other externally-applied heat flux over thirty or more days. Numerical modeling of contrast wettability also showed that a 10-20% inclusion of hydrophobicity reduced the characteristic length and the subsequent evaporation rate (Shokri, et al., 2009). In contrast, from mono-porous media (Chakraborty and Derby, 2018, Chakraborty, et al., 2018) and 2D, hydrophilic or hydrophobic porous network (Chapuis and Prat, 2007), the evaporation rate was ~0.8-1.4 times and 20% faster respectively in hydrophilic media than hydrophobic one.

During evaporation from porous media, liquid islands are formed between two or more adjacent particles (De Vries, 1958, Philip and De Vries, 1957) and they are susceptible to form in hydrophilic media than hydrophobic due to pinning quality of the former. During evaporation, liquid droplets on flat hydrophilic surfaces were found to be pinned (i.e., no change in solid-liquid contact line) while the contact angle gradually decreased (Birdi, et al., 1989, Orejon, et al., 2011, Uno, et al., 1998). In a single pore created with three glass or Teflon spheres, liquid islands formed faster (~1.5 times) in hydrophilic glass than hydrophobic Teflon. The droplet was pinned in one

hydrophilic sphere while in hydrophobic pore, droplet was depinned in all three spheres (Chakraborty and Derby, 2020). In a study of evaporation from randomly packed glass spheres (hydrophilic), different form of liquid island (i.e., capillary bridge, trimmer, pentamer and tetrahedra) were formed among multiple spheres (Scheel, et al., 2008).

Evaporation from porous media depends on porous structure, wettability and formation of liquid island which contribute to maintain hydraulic connection and eventually accelerate the evaporation process. In this study, evaporation of water has been studied and analyzed from two different wettable homogeneous porous column made with hydrophilic glass or hydrophobic Teflon spheres (2.38-mm-diameter). The specific objectives of this research are to: (1) analyze evaporation phenomena from homogeneous porous media based on different evaporation stages and analyze impacts of wettability on evaporation with external heat flux, (2) observe drying front propagation during evaporation by X-ray imaging, (3) analyze diffusion-controlled evaporation at later stage (i.e., slow rate) of evaporation, (4) evaluate effects of wettability on liquid island formation and hydraulic connection, and (5) calculate non-dimensional heat transfer and capillary numbers, and compare them with previous studies to understand evaporation phenomena and properties of porous structure.

2. Experimental procedure

The experiments were done in a systemic procedure where the experimental apparatuses were calibrated and connected according to the schematic diagram (Fig. 2) to record the data, and later the data were post-processed using multiple software (MATLAB, ImageJ, MathCAD) and analytical calculation.

2.1 Experimental apparatus

Evaporation of deionized water was studied from a porous column created with hydrophilic glass or hydrophobic Teflon 2.38-mm-diameter spheres placed in a 1.88-cm-inner-diameter, 6-cm-height and 0.126-cm-thickness cylindrical borosilicate glass beaker. Experiments were conducted in an atmospheric, quiescent atmosphere where the mean relative humidity (RH) was 60% ±1% and the temperature was 22.2° C. An OM-24 multiuse PDF temperature and humidity data logger (± 0.5°C of temperature and ±3% of RH) was used to record and monitor the lab relative humidity and temperature. Fig. 1 shows the average temperature and RH recorded for the experiment for all

replications. The beaker filled with spheres was placed on a sensitive scale (A&D FX-1200i) which has a maximum capacity of 1200 g with ± 0.01 g of uncertainty, which was used to measure the mass of the test section and subsequent mass loss of water during evaporation. Initially, the beaker was placed on the scale and the mass was measured (i.e., 10.04 grams) and subsequently it was filled with ~1165 glass or Teflon spheres.

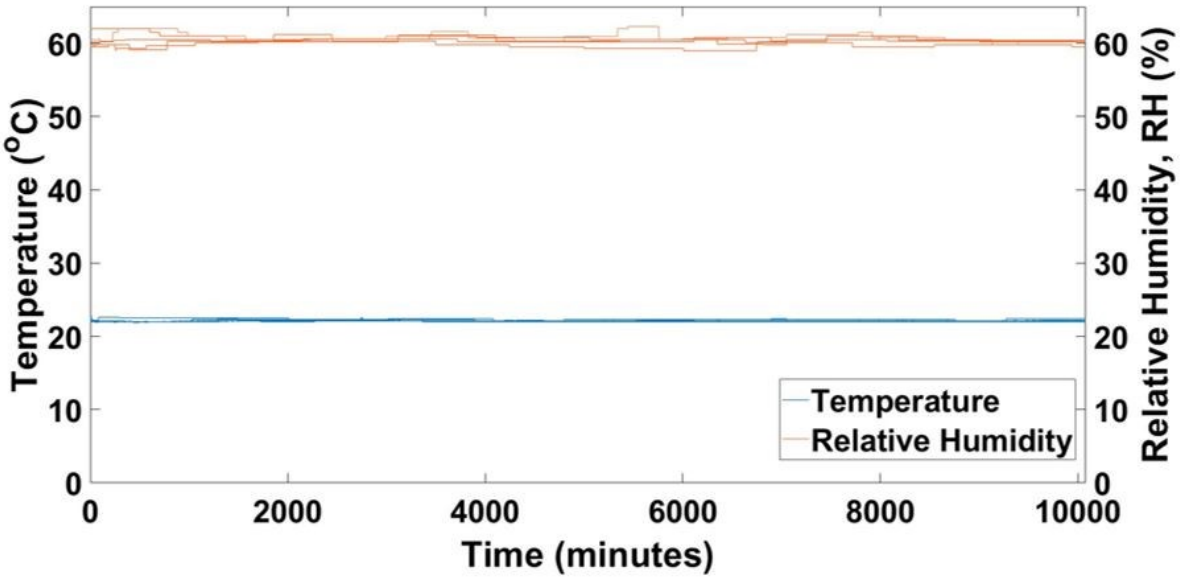

Fig. 1: Average temperature and Relative Humidity (RH) of the experimental atmosphere where the temperature was 22.2°C and RH = 60% ±1%

An Abet LS-10500 solar simulator was used to apply an external heat flux. A DC Xenon-arc lamp (Ushio UXL-150MO) inside the solar simulator produced simulated solar light. The intensity of the produced flux can be manually adjusted, and the intensity is inversely proportional to the beam diameter as well as the distance from top surface of the test sample to the source of light. In this experiment, a heat flux of approximately 1000 W/m^2 was applied and the beam size was maintained at ~22 mm. A 90° beam tuner was used to apply the beam in a vertical position and impinge on the beaker. The heat flux produced by the solar simulator was measured with a 2.36-cm-diameter and 3.63-cm-high LI-COR LI-200R pyranometer with a sensitivity of 75-µA per 1000 W/m^2. The output of the pyranometer was measured with a LI-COR LI-2500A light meter and it was used at the beginning of the experiment to adjust the output heat flux (i.e., 1000 W/m^2) of the solar simulator.

To observe the drying front propagation during evaporation, X-ray imaging was used to capture images at certain time intervals (from third day until the end of each replication at 24 hours

interval). The X-ray generator (EPX-Ecotron) had a square opening of 8 cm by 8 cm which was operated at 40 keV and 20 mAs. The detector (Perkin-Elmer flat panel detector) had a square dimension of 20 cm by 20 cm which obtained images with an exposure time of 250 ms.

Fig. 2 shows the schematic diagram of experimental apparatus. The distance between the X-ray generator and detector was maintained at 30 cm. The scale was placed in front of X-ray detector and the beaker was placed on the top of scale with a negligible distance (i.e., 2 mm) from the X-ray detector to capture better quality image. The distance between the solar simulator and the top surface of the beaker was maintained at approximately 6 cm.

At the beginning of the experiment, the beaker was filled with glass or Teflon spheres and placed on the top of the scale and under the illuminated solar simulator beam. An initial image was captured using an X-ray. Then, 5.8 mL of deionized water was added to the beaker filled with spheres with a volumetric syringe dropper and the sample was tapped continuously to remove air bubbles. From that point, the experiment commenced, and images were captured from the third day of experiment until the end of replication at 24 hours' time interval by X-ray generator. RSMulti software was used to record evaporative mass loss at 5 minutes' interval. Approximately 2 mm (i.e., 0.033 portion of total height) of free water was present on the top of each sample to initiate a constant evaporation rate. In the test sample (the beaker), adding one more layer with spheres would exceed the beaker height (60 mm) and the free 2-mm height was filled with water (i.e., 2-mm free water). For each replication, the experiment's duration was seven days, and five replications were conducted for both glass and Teflon samples.

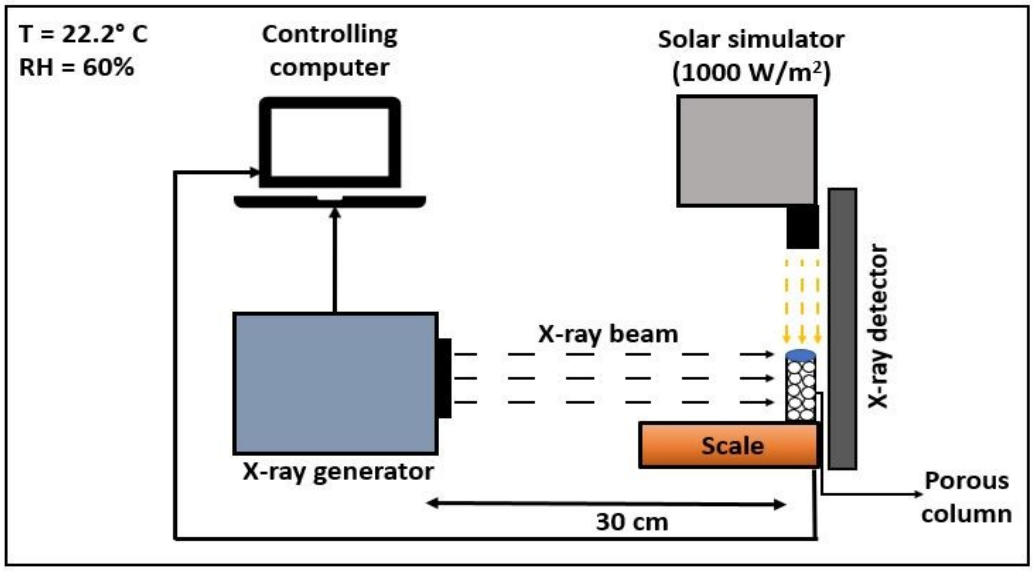

Fig. 2 Schematic of the experimental apparatus in a controlled place where T = 22.2° C and RH = ~60%

2.2 Physical properties of glass and Teflon spheres

Borosilicate glass and PTFE (Polytetrafluoroethylene) spheres with nominal diameter of 2.38 mm were used in these experiments. Spheres were procured from same supplier [McMaster-Carr (Part number: 8996K21 and 9660K21, respectively)]. According to the manufacturer, the spheres have 99.90% sphericity with diameter tolerance of ± 0.0051 mm and ± 0.051 mm for glass and Teflon, respectively. For validation, ten random glass or Teflon spheres were measured with a digital caliper and the mean diameter was found 2.378 mm (± 0.0042 of standard deviation) for glass and 2.377 mm (± 0.0041 of standard deviation) for Teflon. Scanning Electron Microscope (SEM) images were captured to observe surface roughness (Fig. 3) with a Zeiss Evo MA10 microscope (accelerating voltage 200 V-30 KV).

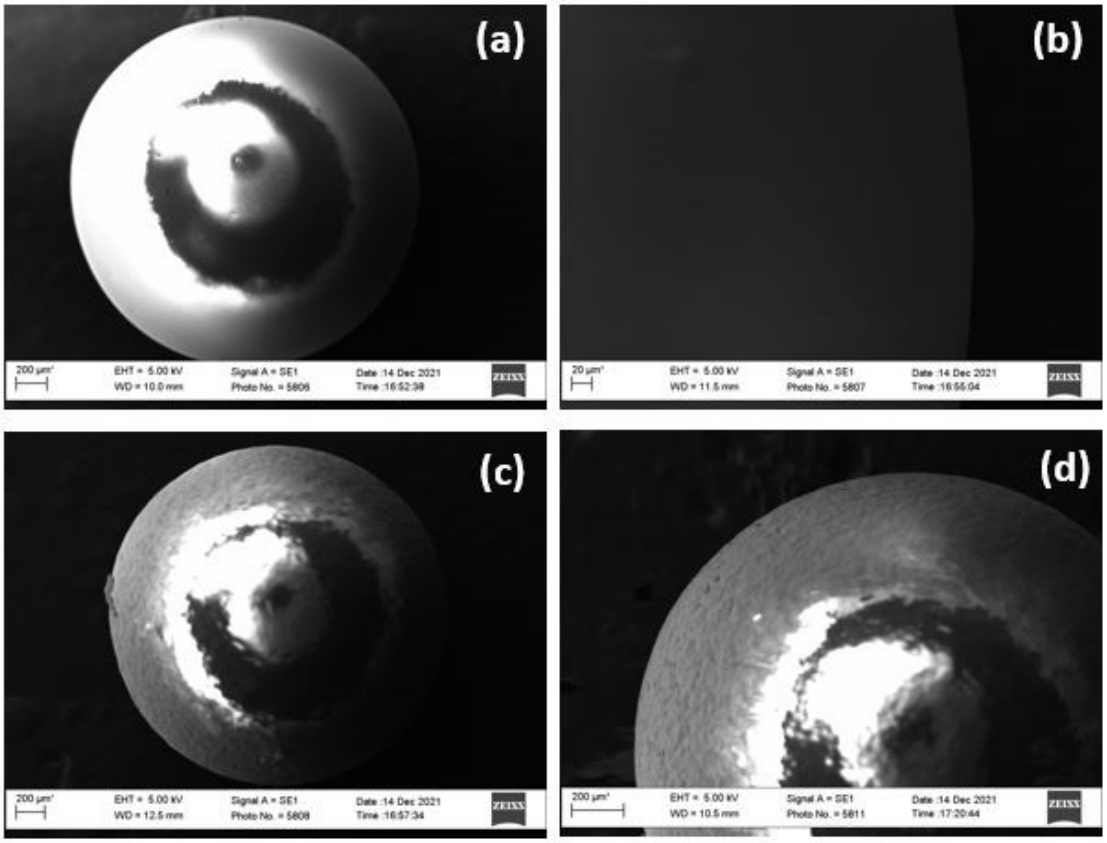

Fig. 3: SEM (Scanning Electron Microscope) images of glass (a and b) and Teflon (c and d) spheres.

2.3 Data post-processing

After finishing the experiment, the mass loss data recorded with the scale were fit into a MATLAB code to generate relations between transient mass loss and porous media properties (e.g., evaporation rate, transient saturation, drying front propagation etc.).

The images taken by X-ray were post-processed using MATLAB where all the pictures were subtracted from the initial reference image (i.e., beaker and spheres with no water). By subtracting from the reference image, the position of the water level and the drying front propagation during evaporation were determined. X-ray image post-processing required consideration of exponential attenuation of X-rays through materials which includes determining the log transform of the image pixel values. The attenuation of x-rays through matter follows the Beer-Lambert law given by:

$$\frac{I}{I_0} = e^{-\eta t} \tag{1}$$

where η is attenuation coefficient, t is the material thickness, I_0 is the x-ray beam intensity, and I is the attenuated x-ray intensity. The detector response, a, is directly proportional to the x-ray intensity, such that a pixel value can be defined in the same way, where C is some constant,

$$a = Ce^{-\eta t}. \quad (2)$$

Assuming the x-ray beam and detector settings to be constant, C will also remain constant, so the material attenuation is directly correlated to the log transform of the pixel value.

For simplicity, b is defined as the log transform of the pixel value,

$$b = log(a). \quad (3)$$

An image of the test section without water (or full of air) is defined as b_a, and an image of the test section full of water is defined as b_w. Assuming a linear relationship between the attenuation of the background and the water, with some algebraic manipulation, the fractional volume of water, V_{frac}, at each location can be calculated by:

$$V_{frac} = \frac{b - b_a}{b_w - b_a} \quad (4)$$

where V_{frac} is fractional volume of water.

3. Results and discussion

In this study, evaporation of water from a porous column created with glass and Teflon spheres of same sizes was analyzed and investigated. The evaporative mass loss was measured and recorded with a sensitive scale and the subsequent evaporative phenomena such as: mass loss, evaporation rate, transient saturation, and drying front depth were analyzed. The X-ray images were captured to understand and localize the evaporative drying front propagation with time and subsequent comparisons were made for glass and Teflon sample.

3.1 Evaporation phenomena

Evaporation phenomena from two different samples were studied and analyzed based on the mass loss data from the scale. The mass loss was recorded at five minutes' time interval for seven days for both sample and they were plotted against time [Fig. 4(a, b)]. The initial mass of water in each sample was 5.8 g and it decreased with time due to evaporative loss. To understand the

difference between glass and Teflon samples, cumulative mass loss was plotted against time in same figure [Fig. 4(a, b)]. After 7 days of experiment, total mass loss was found greater in glass (i.e., ~3 g) than Teflon (i.e., ~2.4 g). A similar trend of mass loss for all 5 replications showed the repeatability of the experimental procedure.

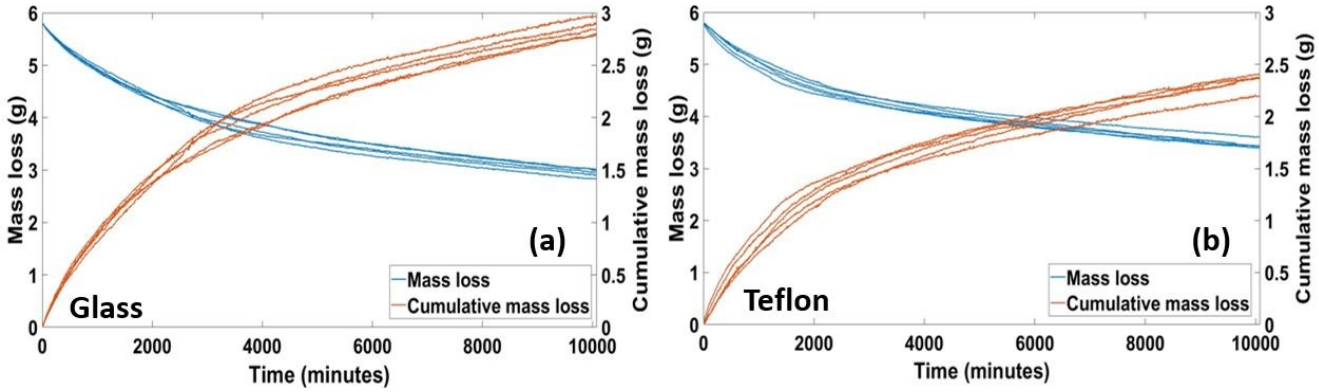

Fig. 4 Mass loss and cumulative mass loss of water from (a) glass and (b) Teflon sample vs. time at 5 minute's intervals. The mass loss of glass is larger (i.e., ~3 g) than Teflon (i.e., ~2.4 g) after seven days of experiment

To distinguish between different evaporation states, transient mass-loss rates and subsequent evaporation rates were calculated. Since each replication took seven days to complete, the averaged mass at one hour increments was used to determine the evaporation rate and the change in mass with respect to time (*dm/dt*). The rate of evaporation was calculated using the following equation:

$$E = \left(\frac{1}{\rho_w A}\right)\left(\frac{dm}{dt}\right) \tag{5}$$

where ρ_w is density of water, A is cross-sectional area of beaker, $\frac{dm}{dt}$ is rate of mass loss and E is rate of evaporation.

The initial evaporation rate was found to be ~7.5 mm/day with a maximum of 0.086 gram/hour mass loss rate in glass sample [Fig. 5 (a) and (c)]. In Teflon [Fig. 5 (b) and (d)], the initial evaporation rate was ~5 mm/day with a maximum mass loss rate 0.06 gram/hour. Comparing both samples, the evaporation rate was approximately 1.5 times higher in glass than Teflon. In these experiments, the constant rate period was almost absent for both glass and Teflon samples. Constant rate depends on heterogeneity and small porous structure which increases capillary action and due to homogeneity and large porous matrix, it was found insignificant in previous studies as well (Borgman, et al., 2017, Nachshon, et al., 2011). Since glass is more wettable than Teflon, the free

water and subsequent layers dried out quickly and experienced a sharp decrease in evaporation rate from the beginning. Due to applied heat flux, each sample experienced a sharp decrease in evaporation rate which is mentioned as falling rate period (Hillel, 1998) where liquid islands are expected to form between multiple particles (De Vries, 1958, Philip and De Vries, 1957, Shokri, et al., 2009).

The falling rate-period lasted longer in glass (until 90th hour) than Teflon (until 70th hour) with a decrease from 5 mm/day to 1 mm/ day, and 3 mm/day to 1 mm/day for glass and Teflon, respectively. The subsequent slower rate period which is controlled by vapor-diffusion (Hillel, 1998, Or, et al., 2013, Shokri, et al., 2009) started for both samples with an evaporation rate of 0-1 mm/day and it lasted until the end of each replication. These evaporation rates are consistent with those in the literature, with observed evaporation rates of 0–0.6 mm/day, 0–1 mm/day, or 0–1.5 mm/day in the slower rate period (Table 1).

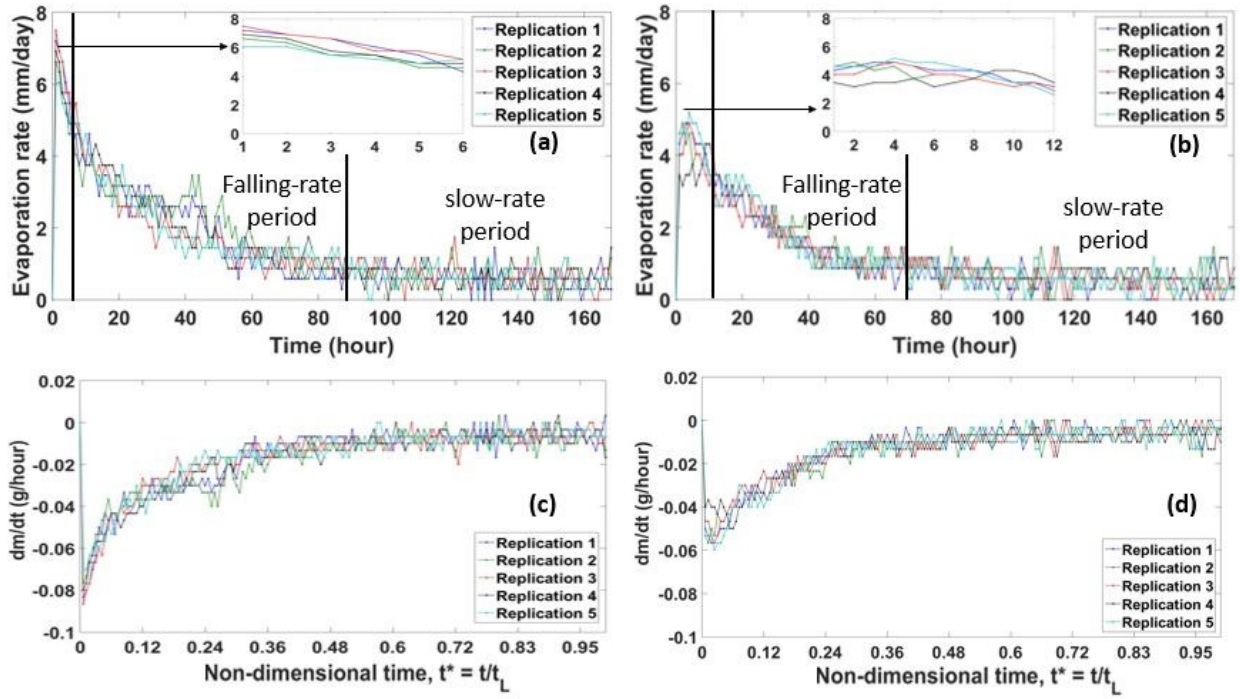

Fig. 5 Evaporation rate and dm/dt vs. time for glass [(a) and (c)] and Teflon [(b) and (d)] sample. Evaporation rates are distinguished into falling-rate and slow-rate period based on the evaporative mass loss. Due to homogeneity constant rate period was absent in both cases. Initial evaporation rate is greater in glass (~7.5 mm/day) than Teflon (~5 mm/day) and the slower rate period started earlier in Teflon (~70 hours) than glass sample (~90 hours). Transient time has been divided by total time, t_L = 168 hours and presented as non-dimensional time, t^* [(c) and (d)]

Table 1: Evaporation rate at slower period in previous studies

Reference	Material	grain diameter (mm)	Sample size (mm) Length, Thickness, width	Evaporation rate at slower rate period (mm/day)
(Shokri, et al., 2008)	Sand	0.3-0.9	260 × 75 × 11	0-1
(Shokri, et al., 2009)	Hydrophilic sand	0.3-0.9	260 × 75 × 11	0-1
	Hydrophobic sand	0.3-0.9	260 × 75 × 11	0-1
(Shokri, et al., 2009)	Sand	0.1-0.5	260 × 75 × 11	0-1
	Sand	0.2-0.3	260 × 75 × 11	0-0.6
(Shokri and Or, 2011)	Quartz sand	0.016-0.717	250 × 75 × 10	0-1
	Glass beads	0.063	250 × 75 × 10	0-1
(Lehmann, et al., 2008)	Fine sand	0.1-0.5	260 × 75 × 10	0-1.5
	Coarse sand	0.3-0.9	260 × 75 × 10	0-1.5

Typically, constant rate of evaporation is associated with two factors: the presence of free water at the top of porous media and the capillary action associated with pore size distribution that supplies water to the evaporative surface defined as characteristic length:

$$L_c = \frac{2\sigma}{\rho_w g}\left(\frac{1}{r_1} - \frac{1}{r_2}\right) \tag{6}$$

where L_c is the characteristic length, σ is the interfacial surface tension, ρ_w is water density, g is acceleration due to gravity, r_1 and r_2 are the smallest and largest drainable pores. Determining the characteristic length leads to predict the duration of constant rate period which is directly dependent on the values of r_1 and r_2, i.e., the pore size distribution. For uniform pores where $r_1 / r_2 = 1$, the characteristic length approaches zero, which leads to an absence or insignificant constant evaporation rate. The uniform spheres' size (2.38 mm) and uniform spheres' distribution led to a uniform porous structure in the overall column which restricted the capillary action in the current scenario.

3.2 Drying front propagation

As the evaporation continues, the evaporative drying front propagates through the porous medium, and the portion of unsaturated area increases. Since the evaporation rate experienced a sharp decrease from the beginning (after short span of constant rate period) and entered the slower

rate of evaporation, the saturation in the transition period could be an important factor to determine evaporation dynamics in a porous medium used in this study. The degree of saturation was determined using the following equation:

$$S = \frac{V_t}{V_i} \tag{7}$$

where V_i is initial water volume and V_t is transient volume of water.

At the end of replication (i.e., after seven days), the saturation of the glass sample was less than 50% which means more than 50% of water evaporated. In contrast, after seven days of experiments with the Teflon sample, the saturation was greater than 60% [Fig. 6 (a and b)]. As, the approximate point for entering slower rate of evaporation have been determined (i.e., ~90 hours for glass, ~70 hours for Teflon), the subsequent saturation was evaluated from the saturation curve [Fig. 6(a and b)]. After the constant rate period, both the sample maintained ~90% of saturation but just before slower rate period, the glass sample maintained nearly 60% saturation where the Teflon sample exhibits 70% saturation and the evaporation rate vs. saturation graph [Fig. 6(c and d)] also exhibits the similar phenomena which implies that Teflon sample entered the slower evaporation period with ~1.2 times more water than glass.

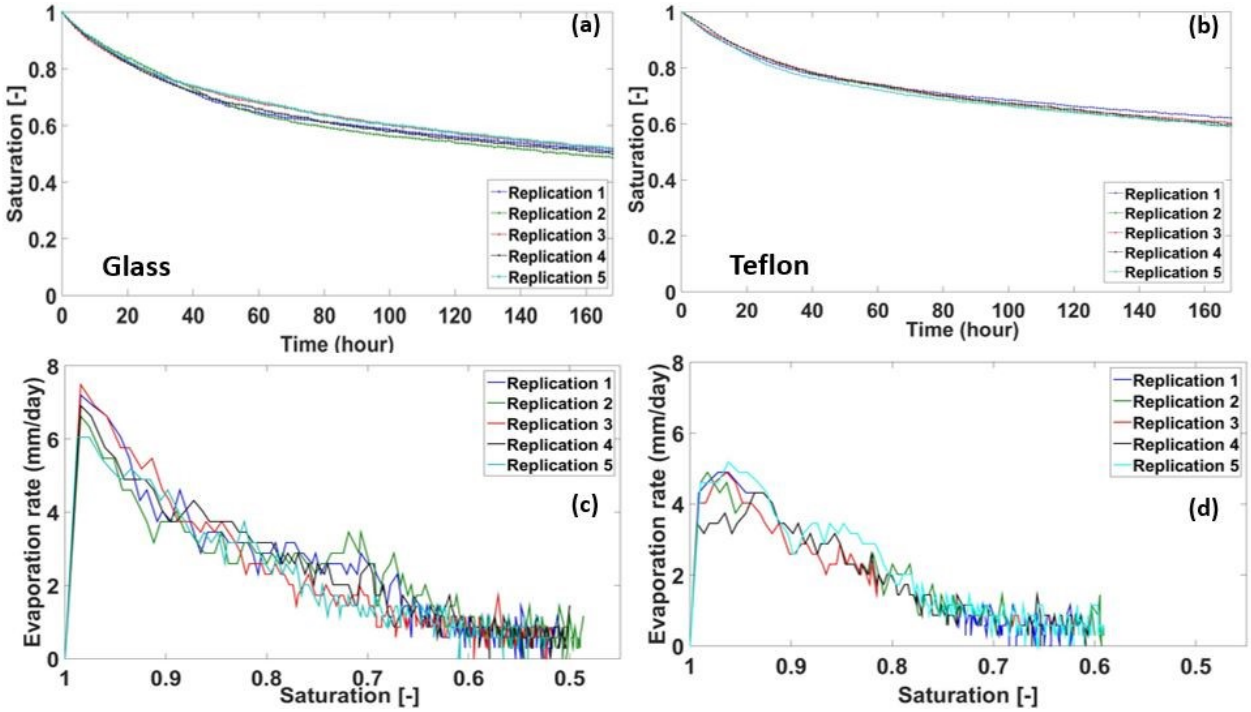

Fig. 6 Saturation vs. time and evaporation rate vs. saturation for glass (a and c) and Teflon (b and d) sample. Almost 10% water was evaporated for both glass and Teflon at constant rate period and approximately 40% and 30% evaporation happened before slower rate starts for glass and Teflon, respectively

As the evaporation continued, the upper portion of the beaker started to become unsaturated as water was lost through evaporation and the drying front progressed. Drying front depth can be defined as the distance from top surface to the final edge of unsaturated part. As the drying front depth increased, the hydraulic linkage between water and evaporative surface was disrupted and the lower rate of evaporation started. In this study, drying front depth was calculated using the following equation:

$$L_D = H(1 - S) \tag{8}$$

where L_D is drying front depth measured from top surface, H is the beaker height i.e., 60 mm and S is transient saturation. The calculated drying front data were plotted against time for both glass [Fig. 7 (a)] and Teflon [Fig. 8 (a)] sample. The drying front at the end of replication was ~30 mm for glass and ~24 mm for Teflon and it propagated slowly in Teflon than glass sample.

X-ray images were captured [Fig. 7 (c) and Fig. 8 (c)] from the third day until end of replication at 24 hours' interval which were post-processed in MATLAB and ImageJ to quantify drying front depth and were plotted [Fig. 7 and Fig. 8 (a), red circle]. To clearly observe the drying front propagation and due to limitations in 2D X-ray, these images were captured from third day of

the experiment. In Fig. 7 and Fig. 8, the color red represents the presence of water (i.e., 100% water saturation), deep blue represents the absence of water (i.e., 0% water saturation), and the color bar represents the range of saturation (i.e., 0 to 1). Drying front depths were obtained using ImageJ; the drying front (marked with black line) was identified where the partially saturated zone meets the fully saturated one and distances were calculated from the bottom to fourteen different points of drying front for each time frame. Then, subtracting those distances from sample height (i.e., 60 mm), the drying front depths were determined and weighted averages were calculated for each time frame was plotted against time [Fig. 7(a) and Fig. 8(a)].

To relate the drying front depth with mass loss of water, the log transform (section 2.3) was used, and the fractional mass loss data were plotted against time [Fig. 7(b) and Fig. 8(b)]. The analytical and experimental data coincided well for both glass and Teflon (Fig. 7 and Fig. 8). As drying progressed, the drying front depth measured from the X-ray images was found greater than the analytical value more often in the glass sample, especially from the 5^{th} to 7^{th} day. Though the drying front propagated deeper, presence of trapped water in form of liquid films among several spheres near the drying front could lead to higher partial saturation (i.e., 0.4-0.5) and subsequent lower values of calculated drying front depth [eqn. (4)] than measured from X-ray. On the contrary, the Teflon sample exhibited a better match between mass loss data (i.e., drying front and fractional mass loss) and X-ray data (i.e., drying front) and the drying front propagated more uniformly than glass, though some partial saturation was observed near the drying front from 3^{rd} until 7^{th} day.

The average fractional mass loss calculated from scale data and X-ray (log-transformed) were then plotted against time. In the glass sample, the fractional mass loss calculated from X-ray was found higher for the last three time frames (i.e., 120, 144 and 168 hours) than the measured mass loss value relating the data with drying front depths [Fig. 7 (a)]; it is postulated that water in liquid islands in the hydrophilic glass sample is the reason for the difference. Liquid islands have been shown to form hydraulic linkages (Lehmann, et al., 2008, Shokri, et al., 2008, Shokri, et al., 2009, Shokri, et al., 2010). In the Teflon sample [Fig. 8 (b)], the fractional mass loss both from x-ray and scale matched well which coincided with the drying front depth [Fig. 8 (b)] which represents the uniformity and lack of liquid networks in the hydrophobic Teflon sample.

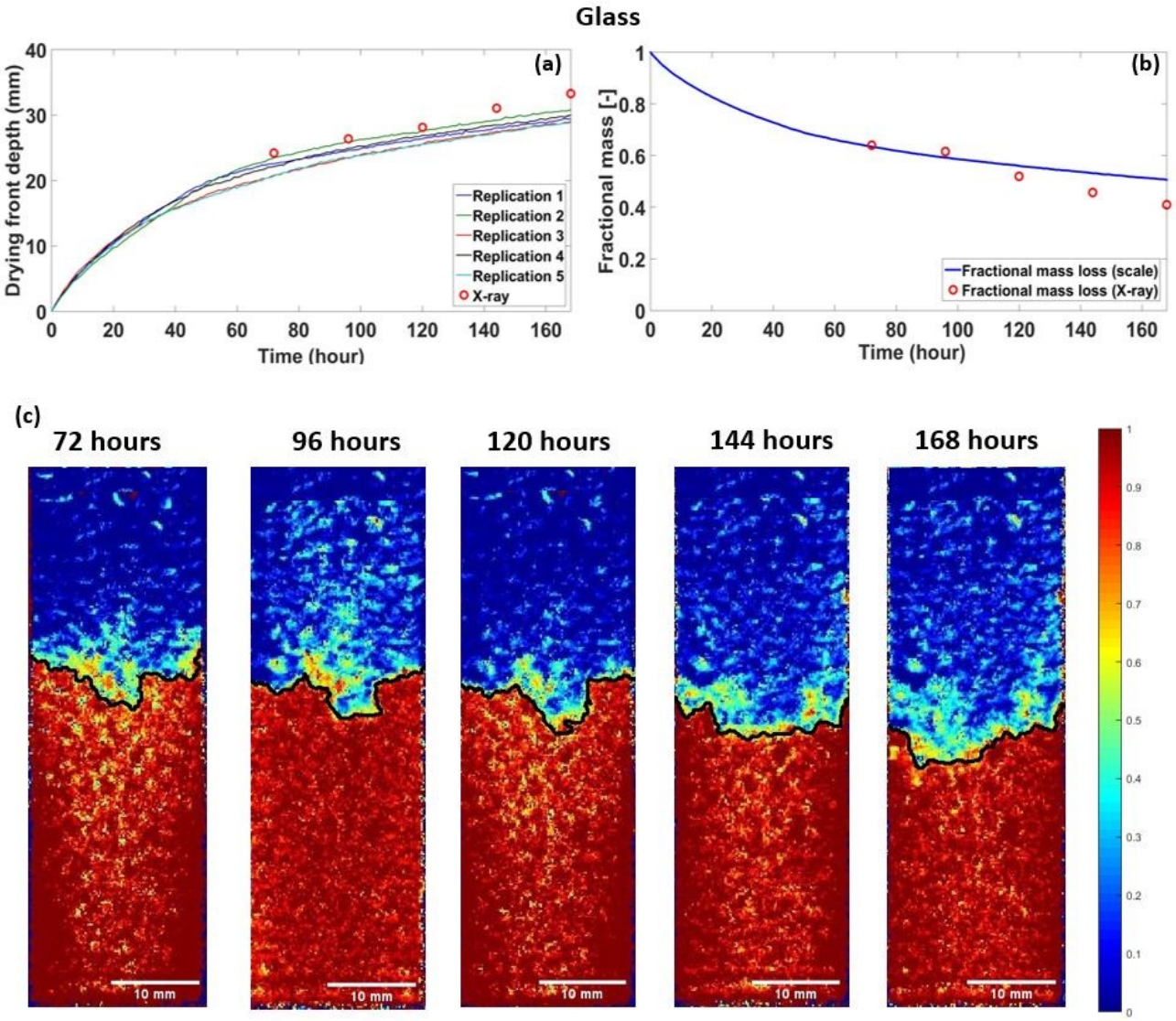

Fig. 7 (a) Drying front depth vs. time and (b) fractional mass loss calculated from scale and x-ray (log-transformed) for glass sample. The bottom pictures (c) show the X-ray imaging of drying front propagation where red and deep blue represents presence (100% water saturation) and absence (0% water saturation) of water respectively. Drying front propagated from ~19 mm to ~34 mm from 3rd day until 7th day. The color bar represents the range of saturation [0-1] and significant partial saturation is observed near the drying front

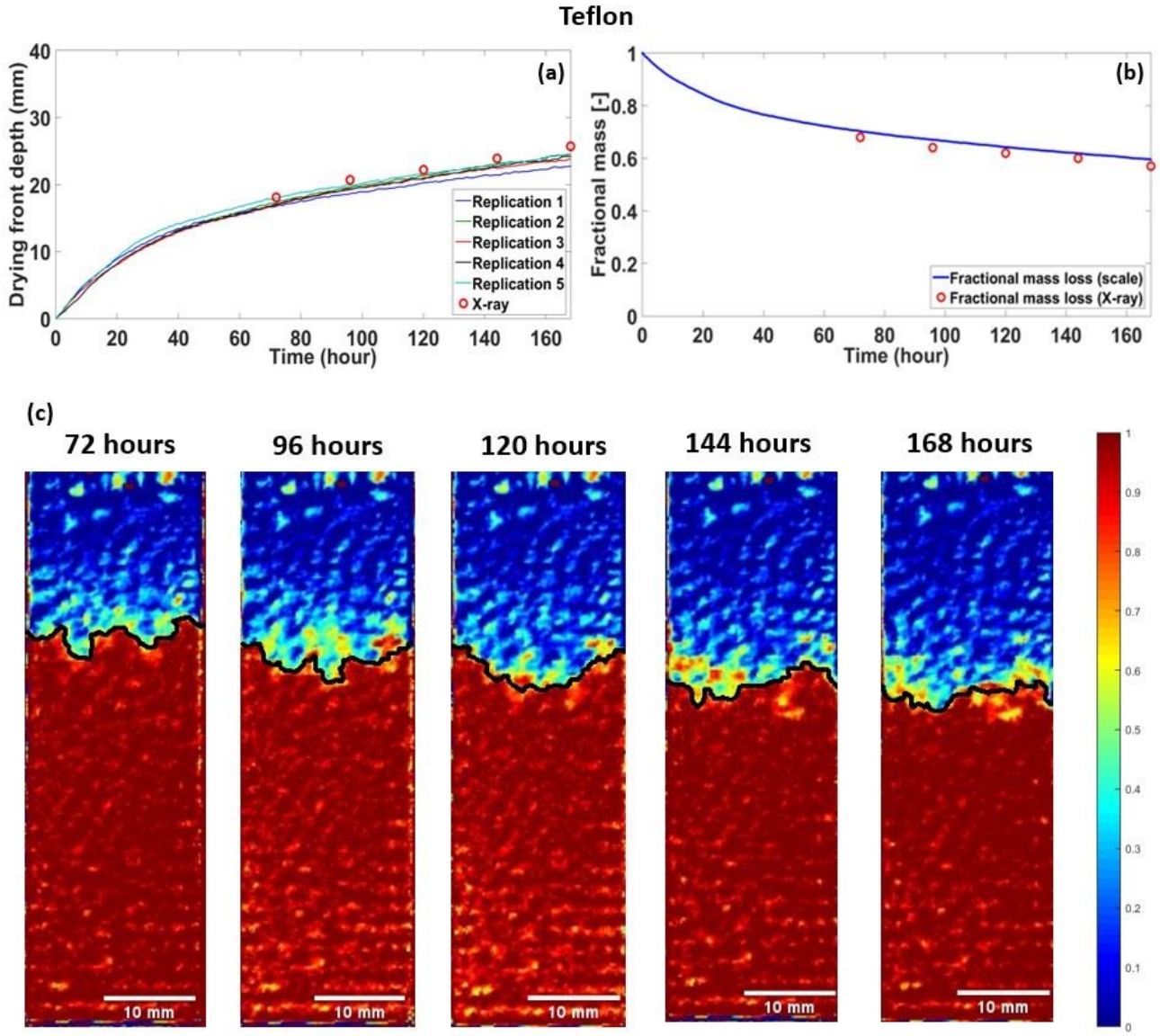

Fig. 8 (a) Drying front depth vs. time and (b) fractional mass loss calculated from scale and x-ray (log-transformed) for Teflon sample. The bottom pictures (c) show the X-ray imaging of drying front propagation where red and deep blue represents presence (100% water saturation) and absence (0% water saturation) of water respectively. The color bar represents the range of saturation [0-1] and some partial saturation is observed near the drying front

When evaporation enters slower rate period, the hydraulic connection breaks down and evaporation is fully dominated by diffusion (Shokri, et al., 2008, Shokri, et al., 2009, Shokri and Or, 2011). The diffusion equation according to Fick's law was presented as driving equation for evaporation:

$$J = \frac{{\theta_a}^{2.5}}{\phi} D \frac{C_{sat} - C_{\infty}}{L_D} \tag{9}$$

$$\phi = 1 - \frac{V_{beads}}{V_{beaker}} \tag{10}$$

where J is diffusive flux, θ_a is volumetric air content, ϕ is porosity, D is water-vapor diffusion coefficient, C_{sat} water-vapor density at evaporating interface, C_{∞} is water-vapor density at atmosphere, L_D is drying front depth, V_{beads} is the total volume of all spheres and V_{beaker} is the volume of beaker. All the variables except the drying front depth are constant for specific fluid at certain temperature, pressure, and relative humidity. Thus, in the slower rate period, vapor diffusion is dependent on drying front propagation. Some assumptions were made for applying the equation (Shokri, et al., 2008, Shokri, et al., 2009, Shokri and Or, 2011): (1) water evaporates from the interface of saturated and unsaturated area i.e., the drying front (2) vapor-diffusion coefficient was computed by the expression of Moldrup et al. (Moldrup, et al., 2000) (3) in the area with no water, volumetric air content is equal to porosity. In the experimental condition: $RH = 60\%, T_{\infty} = 22.2℃, T_{surface} = 27℃$, porosity, $\phi = 0.49$. For calculating the evaporation rate, the diffusive flux was divided with density of water and the unit was converted to mm/day. The saturated water-vapor density, C_{sat}, was calculated for a $T_{surface}$ of 27ºC, and subsequent pressure (3567 Pa) and specific volume [$v_{sat} = 38.774\ m^3/kg$; (Moran, et al., 2010)] using:

$$C_{sat} = \frac{1}{v_{sat}}. \tag{11}$$

Calculated diffusive fluxes were plotted against time along with evaporation rate for both glass and Teflon (Fig. 9). In previous research (Shokri, et al., 2009, Shokri and Or, 2011), evaporation was controlled by vapor diffusion in slow rate period. In this study, slower rate of evaporation starts from ~70 hours and ~90 hours for glass and Teflon, and from that point, the diffusive flux data made well agreement with the evaporation rate. Due to breaking of hydraulic connectivity, evaporation becomes fully dominated by vapor diffusion and the current result shows validation of the model predicted in previous research (Shokri, et al., 2009, Shokri and Or, 2011).

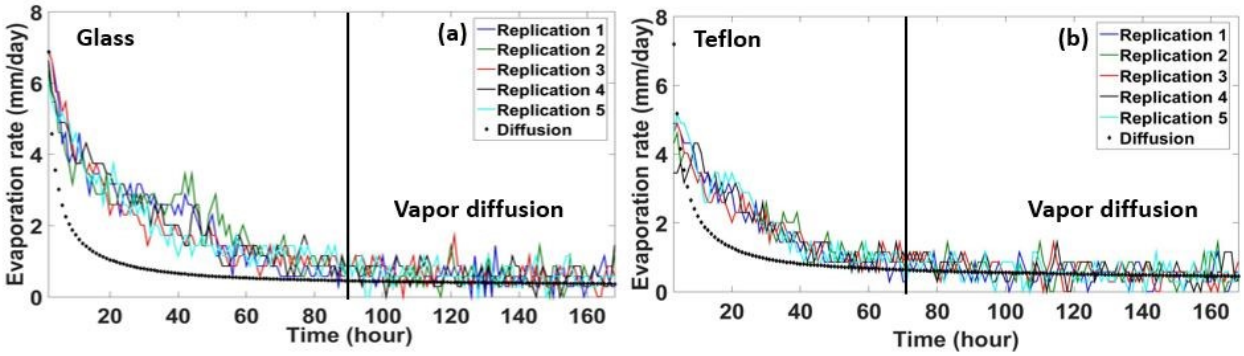

Fig. 9 Diffusive flux (Fick's law) and evaporation rate for glass and Teflon. Diffusive flux match well with evaporation rate after evaporation enters slower rate period for both and glass (After 90 hours) and Teflon (After 70 hours)

3.3 Comparison based on wettability effects and formation of liquid islands

Experiments were conducted to investigate water penetration into hydrophilic and hydrophobic single pores, as liquid transport is an important mechanism in evaporation. Significant differences have been found from the previous experimental analysis where the mass loss rate (~1.25 times) and evaporation rate (~1.4 times) were faster and drying front propagated more quickly in glass than Teflon. To understand and distinguish between the wettability of glass and Teflon, a droplet penetration test was carried out in a single pore created with three touching glass or Teflon spheres. A 2-µL droplet was placed in the pore by a volumetric (0.2-2μL) pipette; 2% green food-coloring was added to the water to get better contrast in imaging. The overall phenomena were captured with a high-speed camera at 30 frame-per-second resolution (Fig. 10).

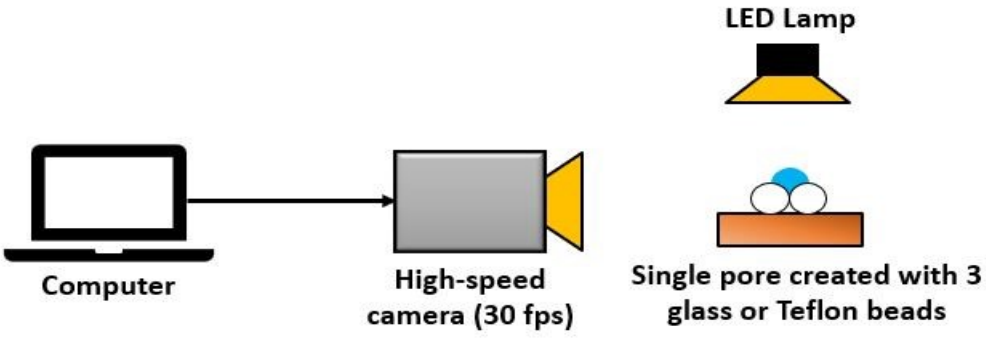

Fig. 10 Schematic of droplet penetration test to understand wettability

The water droplet wetted the glass pore and penetrated it within 0.6 s [Fig. 11 (a-f)], while in a similarly sized Teflon pore, the droplet sat on the top for 10 minutes and completed full penetration after 23 minutes [Fig. 11 (i-n)]. This faster wetting phenomenon in glass spheres also impacts the formation of liquid islands. In single or multi-porous media, liquid islands are susceptible to form between adjacent particles (Chakraborty and Derby, 2020, Chen, et al., 2018, De Vries, 1958, Philip and De Vries, 1957). Typically, liquid islands are formed between two particles when the saturation of the sample starts to decrease leading to a lower evaporation rate. Formation of multiple liquid islands creates hydraulic chain from the saturated to the unsaturated part and the continuation of evaporation happens even if the drying front propagates much deeper with time.

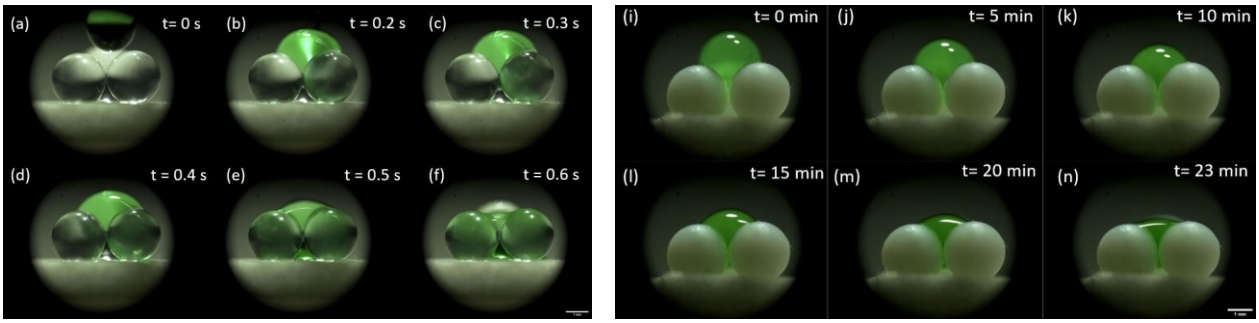

Fig. 11 Droplet penetration test for glass (a-f) and Teflon (i-n) creating a single pore with 3 spheres touching themselves. In glass sample, the droplet penetrated the single pore in less than a second, where in Teflon it took around 23 minutes to penetrate

Liquid islands, also called liquid bridges, are characterized as a liquid connection between two or three particles (Fig. 12) when the test sample (i.e., soil/porous media) becomes partially saturated with decline in water level and evaporation becomes limited with capillary action-driven diffusion (De Vries, 1958, Philip and De Vries, 1957, Scarfone, et al., 2020, Shahraeeni and Or, 2010). In a situation with an imposed heat flux and therefore an imposed temperature gradient, condensation occurs in one side of liquid island and evaporation occurs in the other, but in isothermal conditions, both sides of liquid island experience evaporation and subsequent decline in radius of curvature (Chakraborty and Derby, 2018).

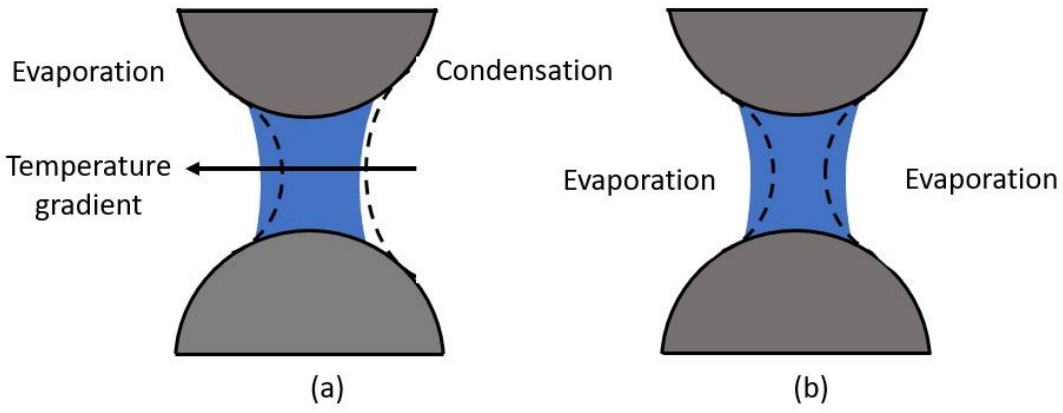

Fig. 12: Liquid island between two particles, (a) due to temperature gradient one side is experiencing condensation and other side is experiencing evaporation, (b) in isothermal condition, both sides are experiencing evaporation

Liquid islands form 1.5x faster in hydrophilic pores than hydrophobic ones and tend to form where liquid can make pinned (i.e., solid-liquid contact lines do not change with time) attachment with the particles (Chakraborty, et al., 2018). On flat hydrophilic surfaces, the solid-liquid contact lines are pinned i.e., the contact area remains same and the contact angle recedes during evaporation, whereas on hydrophobic surfaces, the contact lines recede and contact angle remains same (Birdi, et al., 1989, Orejon, et al., 2011, Uno, et al., 1998), and similar pinning behavior was observed in a single pore (Chakraborty and Derby, 2020). In a multi-porous media, liquid islands are more prone to form in a wettable porous structure and with increasing liquid island, hydraulic linkages can be maintained throughout the evaporative column, resulting in higher evaporation rates (Shokri, et al., 2009). Shokri et al. (2009) observed the primary drying front propagating with time, while a secondary drying front occurred in the partially saturated zone facilitated by small liquid islands. The two drying fronts maintained a hydraulic connection and, in the falling rate evaporation period, both diffusion and simultaneous liquid linkages with the top surface created faster evaporation.

In this study, since glass is more wettable than Teflon, liquid islands are susceptible to form more in glass than Teflon, leading to a creation of hydraulic chain and subsequent faster evaporation (~1.4 times). This phenomenon can also be verified from the X-ray images and drying front graphs (Fig. 7, Fig. 8). Drying front depths measured from the X-ray images were found higher [Fig. 7 (a)] for three time frames (i.e., 120, 144, and 168 hours) than the calculated value while the fractional

mass loss calculated from log-transformed images replicated the similar scenario [Fig. 7 (b)]. In addition, the saturation colormap indicated presence of partial saturation throughout the sample, mostly near the drying fronts [Fig. 7 (c)]. On contrary, drying front propagated more uniformly in Teflon [Fig. 8 (c)] creating a better match in drying front depths [Fig. 8 (a)] and fractional mass loss [Fig. 8 (b)] data. This could imply that, though the 2D drying front depth seemed to be increased from X-ray images, there could still be some water present in the middle creating liquid islands and subsequent hydraulic linkage leading to a faster evaporation in glass.

3.4 Non-dimensional numbers and theoretical modeling

3.4.1 Rayleigh-Nu correlation and calculation (fully saturated)

Evaporation of water under natural convection from porous media has been quantified utilizing non-dimensional numbers to describe the evaporation dynamics both theoretically (Boelter, et al., 1946, Bower and Saylor, 2009, Goldstein, et al., 1973, Lloyd and Moran, 1974, Suzuki and Maeda, 1968) and experimentally (Kumar and Arakeri, 2018, Kumar and Arakeri, 2019). Boelter et al. (1946) investigated free evaporation of water from a free horizontal surface and validated the correlation of Nusselt and Grashof numbers. Lloyd and Moran (1974) established the correlation for Sherwood and Rayleigh numbers for natural convection from porous media,

$$Sh = 0.54Ra^{\frac{1}{4}} (2.2 \times 10^4 \leq Ra \leq 8 \times 10^6) \tag{12}$$

$$Sh = 0.15Ra^{\frac{1}{3}} (8 \times 10^6 \leq Ra \leq 1.6 \times 10^9) \tag{13}$$

where Sh is Sherwood number and Ra is Rayleigh number. Bower and Saylor (2009) theoretically analyzed the correlation between Sherwood and Rayleigh numbers for natural convection-driven evaporation phenomena. The Rayleigh number was defined as:

$$Ra = \frac{g(\rho_w - \rho_\infty){L^*}^3}{\bar{\rho}\upsilon\alpha} \tag{14}$$

where g is acceleration due to gravity, ρ_w is saturated water-vapor density at evaporative front, ρ_∞ is water-vapor density at ambient, $L^* = \frac{A}{P}$, is characteristic length, A and P are surface area and wetted perimeter, $\bar{\rho}$ is average of ρ_w and ρ_∞, υ and α are kinematic viscosity and thermal diffusivity

of air. Goldstein et al. (1973) modeled and considered natural evaporation of water from free surface as like convection from horizontal flat plate and implemented the following Nu-Ra correlation:

$$Nu = 0.59\ (Ra)^{1/4}, 200 < Ra < 10^4 \quad (15)$$

$$Nu = \frac{hL^*}{k_a} \quad (16)$$

where h is convective heat transfer coefficient, k_a is thermal conductivity of air and D is mass diffusivity. Mass diffusivity is derived from the following equation (Incropera, et al., 2007),

$$D = D_{298K}\ (\frac{T}{298})^{3/2}. \quad (17)$$

Suzuki and Maeda (1968) theoretically modeled natural evaporation of water from granular beds by analyzing *Ra-Nu* correlation and Kumar and Arakeri (2018, 2019) experimentally determined the Rayleigh and Nusselt numbers. Comparative study of Rayleigh and Nusselt number calculation of present work with Kumar and Arakeri (2018) is presented in Table 2. Equation (17) and (18) have been used for all cases to make the comparison. The calculated Rayleigh number was 2380 and resulting Nusselt number was 4.1. These values are the same order of magnitude as those found by Kumar and Arakeri (2018), although that study had a higher temperature gradient and higher relative humidity (Table 3).

Table 2: Ra, Nu calculation for natural evaporation for fully saturated state

Reference	Porous material	Surface Temperature (° C)	Ambient Temperature (° C)	RH (%)	*Ra* [-]	*Nu* [-]
Kumar and Arakeri (2018)	Glass plate	38	26.7	69.3	1540	3.7
	Cover slip	37.9	26.4	72.7	883	3.2
Present work	Glass/ Teflon spheres	27	22	60	2380	4.1

Table 3: Corresponding parameters to calculate *Ra, h, Nu*	
Saturated temperature, T_{sat}	27° *C* or 300 *K*
Density difference, $\Delta\rho$	0.014 kg/m^3
Gravitational acceleration, g	9.8 m/s^2
Characteristic length, L^*	0.0047 *m*
Mass diffusivity (25° C), D_{298K}	2.6E-5 m^2/s
Mass diffusivity, D	2.56E-5 m^2/s
Thermal conductivity, k_a	0.02529 *W/m-k*
Rayleigh number, Ra	2380
Heat transfer coefficient, h	22.2 W/m^2-*k*
Nusselt number, Nu	4.1

3.4.2 Bond number, Capillary number and Permeability calculation

To understand the relationships between capillary force with gravitational and viscous forces, Bond and Capillary numbers were calculated using following equations (Cejas, et al., 2017, Yiotis, et al., 2012, Yiotis, et al., 2012):

$$Bo = \frac{\rho_L g {r_{avg}}^2 \sin\theta_{tilt}}{\sigma} \tag{18}$$

$$Ca = \frac{3\pi\mu D C_{sat}}{\sigma\rho_L r_{avg}} \tag{19}$$

where ρ_L is density of liquid, g is acceleration due to gravity, σ is interfacial surface tension, r_{avg} is average bead radius, θ_{tilt} is sample tilt angle, μ is dynamic viscosity, D is diffusion co-efficient, C_{sat} is saturated vapor concentration. The interfacial tension was calculated from the following equation (Carey, 2018):

$$\sigma = 235.8(1 - \frac{T_{sat}}{T_c})^{1.256}[1 - 0.625(1 - \frac{T_{sat}}{T_c})] \quad (20)$$

Bond number depends on the liquid properties (i.e., density, interfacial tension) and average beads radius and it increases with increased beads size (Cejas, et al., 2017, Rogers and Kaviany, 1990, Yiotis, et al., 2012) and the Bond number in this study was found 193E-3 for 1.19 mm of beads radius. Table 4 represents the comparative study of Bond and Capillary number estimation of previous results with this study. Yiotis, et al., 2012 and Cejas, et al., 2017 analyzed some effects of tilt angle on Bond number, but to compare with this study, only tilt angles of 90° were considered. Instead of average beads radius, r_{avg}, effective pore radius, r_{eff}, was used in one study (Kumar and Arakeri, 2019) and subsequent lower value of Bond numbers were found (i.e., 2.34E-3 – 2.48E-3). For Capillary number calculation, the model predicted with rounded-corner films was used in this study and a value of 6.203E-8 was found. In some studies (Chen, et al., 2018, Kumar and Arakeri, 2019), Capillary number was calculated as a function of constant evaporation rate, but due to insiginificant constant rate, in this study, capillary number was calculated as a function of average beads radius.

Table 4: Bond and Capillary number calculation for different studies

Reference	Porous media material	Average beads radius (mm)	Working fluid	Bo number, Bo [-]	Capillary number, Ca [-]
(Rogers and Kaviany, 1990)	Glass beads	0.1	Water	1.4E-3	Not reported
		0.5	Water	33.7E-3	
		1.5	Water	302E-3	
(Yiotis, et al., 2012)	Glass beads	0.065	n-Pentane/ n-Hexane	1.62E-3	8520E-8
		0.225	n-Pentane/ n-Hexane	19.5E-3	2460E-8
(Cejas, et al., 2017)	Glass beads	0.25	Water	9.1E-3-49E-3	0.85E-8-4.93E-8
		0.5	Water	36.2E-3-196E-3	0.89E-8-3.33E-8
(Kumar and Arakeri, 2019)	Glass beads	0.35	Water	2.34E-3	6.19E-8
		0.425	Water	2.48E-3	4.67E-8
Present work	Glass beads	1.19	Water	193E-3	6.203E-8

To calculate the permeability of a porous media created with uniform spheres, the following RGPZ (Revil, Glover, Pezard, and Zamora) model was proposed (Glover, et al., 2006, Johnson, et al., 1986):

$$k = \frac{\Lambda^2}{cF} \tag{21}$$

where k is permeability, Λ is characteristic pore radius, c is pore shape factor, and F is formation factor, where Λ and F are expressed by following equations:

$$\Lambda = \frac{d}{2mF} \tag{22}$$

$$F = \phi^{-m} \tag{23}$$

where d is representative grain diameter, m is cementation exponent, and ϕ is porosity. For spherical particles, m = 1.5 and c = 8/3. The model was validated for 15 spherical uniform glass beads packing (Glover and Walker, 2009, Glover, et al., 2006) and the following equations were used to introduce effective pore radius within same permeability model:

$$\Theta = \sqrt{\frac{cm^2F^2}{8}} \tag{24}$$

$$\Lambda = \frac{\Theta\, r_{eff}}{mF} = r_{eff}\sqrt{\frac{c}{8}} \tag{25}$$

$$k \approx \frac{\Lambda^2}{cF} = \frac{{r_{eff}}^2}{8F} \tag{26}$$

where Θ is theta transform (unitless) and r_{eff} is effective pore radius. Additionally, CPA (Critical Path Analysis) was proposed in a study as an alternate method to predict permeability (Ghanbarian, 2020), which can be used for homogeneous spherical porous system and the predicted model matched well with the measured permeability with RMSLE (Root Mean Square Log-transformed Error) 0.16. In this model, the critical diameter $d_c = 0.42\overline{D}$, where $\overline{D}$ is average bead's diameter. The permeability is expressed as following equation:

$$k = \frac{{d_c}^2}{CF} \tag{27}$$

where, C is a constant co-efficient and for spherical mono-disperse particle, the value was set as 72.2 which produced significantly better (RMSLE=0.16) permeability results. Using, these two above-mentioned models, the permeability of this study was achieved as $k(RGPZ) = 3.163E-9\ m^2$ and $k(CPA) = 3.287E-9\ m^2$. In a study (Glover and Walker, 2009), using glass beads of several sizes, permeability was calculated using the RGPZ model and the following table demonstrates the permeability results of previous and this studies:

Table 5: Calculation of permeability for previous and this study

Reference	Effective grain diameter, (μm)	Cementation exponent, m	Porosity, ϕ	Effective pore radius, μm	Permeability, k (m^2)
Glover, et al., 2006	1000 ± 34	1.56 ± 0.005	0.3954	150.6±10.2	0.724E-9
	2000 ± 67	1.49 ± 0.005	0.3856	281±18.9	2.386E-9
	3350 ± 184	1.48 ± 0.005	0.3965	498.5±44.2	7.902E-9
Glover and Walker, 2009	3000 ± 154	1.56 ± 0.005	0.3978	395.4±32.9	4.638E-9
	4000 ± 198	1.55 ± 0.005	0.3854	509.84±41.7	7.411E-9
Present work	2380	1.5	0.477	326.4	3.163E-9 (RGPZ) 3.287E-9 (CPA)

To measure the permeability of the porous beads, hydraulic conductivity was measured using a constant head technique (Figure 13) and the relationship between hydraulic conductivity and permeability was used to calculate experimental permeability. A total of 1300 spheres (i.e., glass and Teflon) were assembled in two 0.254-m-diameter and 0.0286-m-tall glass tubes (with both sides open) to create the porous sample. Metal meshes were fixed on both sides of the tube to hold the spheres in place and allow water to pass through. Water was placed in a reservoir tank (l = 0.42 m, w = 0.3 m, h = 0.17 m), which was sufficiently large to maintain a near-constant pressure head. A 0.24 m long plastic tube with inner diameter of 0.254 m was used to connect the tank with the porous sample. Initially, the water head was maintained at 0.42 m and the water passed through the porous sample for 10 seconds via gravity. Each sample was tested five times, and for each trial, the water was collected in a collecting tank and the mass was measured in real-time using a scale. From the mass of water collected the flow rate was measured and the hydraulic conductivity was calculated using the following equations:

$$K = \frac{Q}{iA} \tag{28}$$

$$Q = \frac{\forall}{t} \tag{29}$$

$$i = \frac{-\Delta h}{L} \tag{30}$$

where, K is hydraulic conductivity, Q is volumetric flow rate, $\forall$ is amount of water collected, t is time, Δh is the pressure head difference, L is height, and A is cross sectional area of the test sample. The following permeability-hydraulic conductivity relationship was used to calculate permeability of the porous system (Chapuis and Aubertin, 2003):

$$k = \frac{K\mu}{\rho g} \tag{31}$$

where, k is permeability, μ is viscosity, ρ is density of water, and g is acceleration due to gravity. The measured permeability of the glass sample was approximately 6% higher, likely due to the hydrophobicity (section 3.3); for glass, the average permeability was found 9.5E-10 m^2 with a standard deviation of 2.7E-11 m^2 and for Teflon, the average permeability was 8.9E-10 m^2 with a 1.21E-11 m^2 standard deviation. (Table 5); measured permeability values are comparable to predictions by the RGPZ and CPA models (Table 6); properties are provided in Table 7.

Table 6: Predicted and measured values of permeability for the porous sample

Predicted		Experimental	
k (RGPZ) (m^2)	k (CPA) (m^2)	k (measured), glass, (m^2)	k (measured), Teflon, (m^2)
3.163E-9	3.287E-9	9.5E-10	8.9E-10

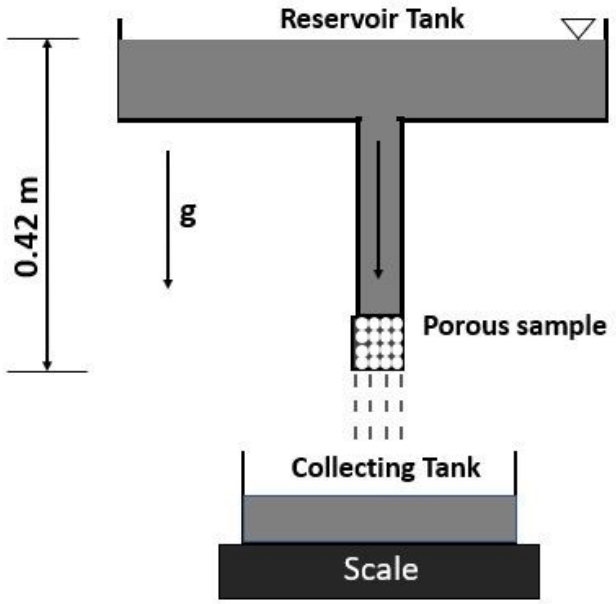

Figure 13: Hydraulic conductivity measurement of the porous system using constant head method

Table 7: Corresponding parameters to calculate Bond number, Capillary Number and Permeability	
Critical temperature, T_c	373.9° *C* or 646.9 *K*
Interfacial Tension, σ	71.672 *mN/m*
Average particle diameter, d	2.38 *mm* or 0.00238 *m*
Porosity, ϕ	0.477
Dynamic viscosity, μ	0.0008502 m^2
Formation factor, F	3.035
Pore shape factor, c	8/3
Cementation exponent, m	1.5
Constant co-efficient, C	72.2 (Ghanbarian, 2020)
Characteristic pore radius, Λ	2.614E-4 *m*
Effective pore radius, r_{eff}	4.527E-4 *m*
Head difference, Δh	16 inch or 0.4064 m
Height of porous sample, L	1.125 inch or 0.029 m

Conclusions

In this study, evaporation of water from homogeneous hydrophilic (i.e., glass) and hydrophobic (i.e., Teflon) porous columns was investigated. After seven days of replication, approximately 25% more water was evaporated from glass (i.e., ~3 g) than Teflon (i.e., ~2.4 g). Due to the larger pore size and homogeneity, capillary action was negligible resulting in a minimal constant evaporation rate period. Evaporation entered into slower rate period (e.g., 0-1 mm/day) preceded by a sharp decrease due to evaporative loss faster in Teflon (~70 hours) than glass (~90 hours). In the slower rate period, evaporation was controlled by Fick's law of diffusion and the calculated evaporation rate matched well with the diffusive flux. The saturation of the Teflon sample was 0.7 while entering into slower rate period than glass (e.g., saturation of 0.6), and the drying front propagated faster in glass than Teflon sample and the final drying front depth after seven days were greater in glass (~30 mm). The mass loss and X-ray data align for the Teflon sample. In contrast, for the glass sample, the fractional mass loss calculated from X-ray was higher for the last three time frames (i.e., 120, 144 and 168 hours) than the measured mass loss value relating the data with drying front depths, suggesting that additional water was present in liquid islands. Rayleigh numbers (Ra=2380) and Nusselt (Nu=4.1) numbers were calculated for quantifying natural evaporation of water from fully saturated porous media. Bond (Bo=193E-3) and Capillary (Ca=6.203E-8) numbers were calculated as a function of average spheres diameter and comparisons were made with other porous media studies. Permeability was calculated by using RGPZ and CPA models and compared it with experimental data. Due to more wettability, the glass sample was susceptible to form more liquid islands, thereby creating a hydraulic connection between saturated and unsaturated parts which led to higher evaporation rate than Teflon. Future work could include modeling of liquid islands and its effect on evaporation from macro- or micro-scale porous media. The effects of heterogeneity on evaporation from porous media represent an interesting opportunity for future work.

Funding

Funding This research was supported by NSF Grants #1651451 and #1828571, and this material is based upon work supported by the Department of Energy under Award DE-NE008690.

References

Aboufoul, M., Shokri, N., Saleh, E., Tuck, C.,Garcia, A.: Dynamics of water evaporation from porous asphalt. Construction and Building Materials. 202, 406-414 (2019).

Bachmann, J., Horton, R.,Van der Ploeg, R.: Isothermal and nonisothermal evaporation from four sandy soils of different water repellency. Soil Science Society of America Journal. 65, 1599-1607 (2001).

Birdi, K., Vu, D.,Winter, A.: A study of the evaporation rates of small water drops placed on a solid surface. The Journal of physical chemistry. 93, 3702-3703 (1989).

Boelter, L., Gordon, H.,Griffin, J.: Free evaporation into air of water from a free horizontal quiet surface. Industrial & Engineering Chemistry. 38, 596-600 (1946).

Borgman, O., Fantinel, P., Lühder, W., Goehring, L.,Holtzman, R.: Impact of spatially correlated pore-scale heterogeneity on drying porous media. Water Resources Research. 53, 5645-5658 (2017).

Bower, S.,Saylor, J.: A study of the Sherwood–Rayleigh relation for water undergoing natural convection-driven evaporation. International Journal of Heat and Mass Transfer. 52, 3055-3063 (2009).

Carey, V.P.: Liquid-vapor phase-change phenomena: an introduction to the thermophysics of vaporization and condensation processes in heat transfer equipment. CRC Press (2018)

Cejas, C.M., Castaing, J.-C., Hough, L., Frétigny, C.,Dreyfus, R.: Experimental investigation of water distribution in a two-phase zone during gravity-dominated evaporation. Physical Review E. 96, 062908 (2017).

Cejas, C.M., Hough, L., Frétigny, C.,Dreyfus, R.: Effect of granular packing geometry on evaporation. arXiv preprint arXiv:1601.04584. (2016).

Chakraborty, P.P.,Derby, M.M.: Evaporation From a Simulated Soil Pore: Effects of Relative Humidity. International Conference on Nanochannels, Microchannels, and Minichannels. 51197, (2018).

Chakraborty, P.P.,Derby, M.M.: 'Evaporation From a Simulated Soil Pore: Effects of Relative Humidity' in Editor (ed.)^(eds.), From *Book Evaporation From a Simulated Soil Pore: Effects of Relative Humidity*, City: American Society of Mechanical Engineers Digital Collection, pp., at. (2018)

Chakraborty, P.P.,Derby, M.M.: Contact Line Pinning and Depinning Prior to Rupture of an Evaporating Droplet in a Simulated Soil Pore. International Conference on Nanochannels, Microchannels, and Minichannels. 83693, (2020).

Chakraborty, P.P.,Derby, M.M.: 'Contact Line Pinning and Depinning Prior to Rupture of an Evaporating Droplet in a Simulated Soil Pore' in Editor (ed.)^(eds.), From *Book Contact Line Pinning and Depinning Prior to Rupture of an Evaporating Droplet in a Simulated Soil Pore*, City: American Society of Mechanical Engineers Digital Collection, pp., at. (2020)

Chakraborty, P.P., Huber, R., Chen, X.,Derby, M.M.: Evaporation From Simulated Soil Pores: Effects of Wettability, Liquid Islands, and Breakup. Interfacial Phenomena and Heat Transfer. 6, (2018).

Chapuis, O.,Prat, M.: Influence of wettability conditions on slow evaporation in two-dimensional porous media. Physical review E. 75, 046311 (2007).

Chapuis, O., Prat, M., Quintard, M., Chane-Kane, E., Guillot, O.,Mayer, N.: Two-phase flow and evaporation in model fibrous media: Application to the gas diffusion layer of PEM fuel cells. Journal of Power Sources. 178, 258-268 (2008).

Chapuis, R.P.,Aubertin, M.: On the use of the Kozeny Carman equation to predict the hydraulic conductivity of soils. Canadian Geotechnical Journal. 40, 616-628 (2003).

Chen, C., Duru, P., Joseph, P., Geoffroy, S.,Prat, M.: Control of evaporation by geometry in capillary structures. From confined pillar arrays in a gap radial gradient to phyllotaxy-inspired geometry. Scientific reports. 7, 1-8 (2017).

Chen, C., Joseph, P., Geoffroy, S., Prat, M.,Duru, P.: Evaporation with the formation of chains of liquid bridges. Journal of Fluid Mechanics. 837, 703-728 (2018).

De Vries, D.: Simultaneous transfer of heat and moisture in porous media. Eos, Transactions American Geophysical Union. 39, 909-916 (1958).

Ghanbarian, B.: Applications of critical path analysis to uniform grain packings with narrow conductance distributions: I. Single-phase permeability. Advances in Water Resources. 137, 103529 (2020).

Glover, P.,Walker, E.: Grain-size to effective pore-size transformation derived from electrokinetic theory. Geophysics. 74, E17-E29 (2009).

Glover, P., Zadjali, I.,Frew, K.: Permeability prediction from MICP and NMR data using an electrokinetic approach: Geophysics (2006).

Goldstein, R.J., Sparrow, E.M.,Jones, D.: Natural convection mass transfer adjacent to horizontal plates. International Journal of Heat and Mass Transfer. 16, 1025-1035 (1973).

Hanlon, M.,Ma, H.: Evaporation heat transfer in sintered porous media. J. Heat Transfer. 125, 644-652 (2003).

Hillel, D.: Environmental soil physics: Fundamentals, applications, and environmental considerations. Elsevier (1998)

Incropera, F.P., Lavine, A.S., Bergman, T.L.,DeWitt, D.P.: Fundamentals of heat and mass transfer. Wiley (2007)

Johnson, D.L., Koplik, J.,Schwartz, L.M.: New pore-size parameter characterizing transport in porous media. Physical review letters. 57, 2564 (1986).

Khrustalev, D.,Faghri, A.: Heat transfer during evaporation on capillary-grooved structures of heat pipes (1995).

Kobayashi, Y., Ikeda, S.,Iwasa, M.: Evaporative heat transfer at the evaporative section of a grooved heat pipe. Journal of thermophysics and heat transfer. 10, 83-89 (1996).

Kohout, M., Grof, Z.,Štěpánek, F.: Pore-scale modelling and tomographic visualisation of drying in granular media. Journal of colloid and interface science. 299, 342-351 (2006).

Kumar, N.,Arakeri, J.H.: Evaporation from layered porous medium in the presence of infrared heating. Water Resources Research. 54, 7670-7687 (2018).

Kumar, N.,Arakeri, J.H.: Experimental and numerical investigation of evaporation from line sources of water in low porosity surfaces. Journal of Hydrology. 569, 795-808 (2019).

Kumar, N.,Arakeri, J.H.: Investigation on the effect of temperature on evaporative characteristic length of a porous medium. Drying Technology. (2019).

Lehmann, P., Assouline, S.,Or, D.: Characteristic lengths affecting evaporative drying of porous media. Physical Review E. 77, 056309 (2008).

Li, Y., He, H.-f.,Zeng, Z.-x.: Evaporation and condensation heat transfer in a heat pipe with a sintered-grooved composite wick. Applied Thermal Engineering. 50, 342-351 (2013).

Lloyd, J.,Moran, W.: Natural convection adjacent to horizontal surface of various planforms (1974).

Mantelli, M.H.: Development of porous media thermosyphon technology for vapor recovering in cross-current cooling towers. Applied Thermal Engineering. 108, 398-413 (2016).

Médici, E.F.,Allen, J.S.: Evaporation, two phase flow, and thermal transport in porous media with application to low-temperature fuel cells. International Journal of Heat and Mass Transfer. 65, 779-788 (2013).

Moldrup, P., Olesen, T., Gamst, J., Schjønning, P., Yamaguchi, T.,Rolston, D.: Predicting the gas diffusion coefficient in repacked soil water-induced linear reduction model. Soil Science Society of America Journal. 64, 1588-1594 (2000).

Moran, M.J., Shapiro, H.N., Boettner, D.D.,Bailey, M.B.: Fundamentals of engineering thermodynamics. John Wiley & Sons (2010)

Nachshon, U., Weisbrod, N., Dragila, M.I.,Grader, A.: Combined evaporation and salt precipitation in homogeneous and heterogeneous porous media. Water Resources Research. 47, (2011).

Onwude, D.I., Hashim, N., Chen, G., Putranto, A.,Udoenoh, N.R.: A fully coupled multiphase model for infrared-convective drying of sweet potato. Journal of the Science of Food and Agriculture. 101, 398-413 (2021).

Or, D., Lehmann, P., Shahraeeni, E.,Shokri, N.: Advances in soil evaporation physics—A review. Vadose Zone Journal. 12, 1-16 (2013).

Orejon, D., Sefiane, K.,Shanahan, M.E.: Stick–slip of evaporating droplets: substrate hydrophobicity and nanoparticle concentration. Langmuir. 27, 12834-12843 (2011).

Philip, J.,De Vries, D.: Moisture movement in porous materials under temperature gradients. Eos, Transactions American Geophysical Union. 38, 222-232 (1957).

Prime, N., Housni, Z., Fraikin, L., Léonard, A., Charlier, R.,Levasseur, S.: On water transfer and hydraulic connection layer during the convective drying of rigid porous material. Transport in porous media. 106, 47-72 (2015).

Prommas, R.: Theoretical and experimental study of heat and mass transfer mechanism during convective drying of multi-layered porous packed bed. International Communications in Heat and Mass Transfer. 38, 900-905 (2011).

Purlis, E.: Modelling convective drying of foods: A multiphase porous media model considering heat of sorption. Journal of food engineering. 263, 132-146 (2019).

Rogers, J.,Kaviany, M.: Variation of heat and mass transfer coefficients during drying of granular beds (1990).

Saneinejad, S., Moonen, P., Defraeye, T., Derome, D.,Carmeliet, J.: Coupled CFD, radiation and porous media transport model for evaluating evaporative cooling in an urban environment. Journal of Wind Engineering and Industrial Aerodynamics. 104, 455-463 (2012).

Scarfone, R., Wheeler, S.J.,Lloret-Cabot, M.: Conceptual hydraulic conductivity model for unsaturated soils at low degree of saturation and its application to the study of capillary barrier systems. Journal of Geotechnical and Geoenvironmental Engineering. 146, 04020106 (2020).

Scheel, M., Seemann, R., Brinkmann, M., Di Michiel, M., Sheppard, A., Breidenbach, B.,Herminghaus, S.: Morphological clues to wet granular pile stability. Nature materials. 7, 189-193 (2008).

Scheel, M., Seemann, R., Brinkmann, M., Di Michiel, M., Sheppard, A.,Herminghaus, S.: Liquid distribution and cohesion in wet granular assemblies beyond the capillary bridge regime. Journal of Physics: Condensed Matter. 20, 494236 (2008).

Shahidzadeh-Bonn, N., Tournié, A., Bichon, S., Vié, P., Rodts, S., Faure, P., Bertrand, F.,Azouni, A.: Effect of wetting on the dynamics of drainage in porous media. Transport in porous media. 56, 209-224 (2004).

Shahraeeni, E.,Or, D.: Pore-scale analysis of evaporation and condensation dynamics in porous media. Langmuir. 26, 13924-13936 (2010).

Shokri, N., Lehmann, P.,Or, D.: Effects of hydrophobic layers on evaporation from porous media. Geophysical Research Letters. 35, (2008).

Shokri, N., Lehmann, P.,Or, D.: Characteristics of evaporation from partially wettable porous media. Water Resources Research. 45, (2009).

Shokri, N., Lehmann, P.,Or, D.: Critical evaluation of enhancement factors for vapor transport through unsaturated porous media. Water resources research. 45, (2009).

Shokri, N., Lehmann, P.,Or, D.: Evaporation from layered porous media. Journal of Geophysical Research: Solid Earth. 115, (2010).

Shokri, N., Lehmann, P., Vontobel, P.,Or, D.: Drying front and water content dynamics during evaporation from sand delineated by neutron radiography. Water resources research. 44, (2008).

Shokri, N.,Or, D.: What determines drying rates at the onset of diffusion controlled stage-2 evaporation from porous media? Water Resources Research. 47, (2011).

Suzuki, M.,Maeda, S.: ON THE MECHANISM OF DRYING OF GRANULAR BEDS Mass Transfer from Discontinuous Source. Journal of chemical engineering of Japan. 1, 26-31 (1968).

Thiery, J., Rodts, S., Weitz, D.,Coussot, P.: Drying regimes in homogeneous porous media from macro-to nanoscale. Physical Review Fluids. 2, 074201 (2017).

Uno, K., Hayashi, K., Hayashi, T., Ito, K.,Kitano, H.: Particle adsorption in evaporating droplets of polymer latex dispersions on hydrophilic and hydrophobic surfaces. Colloid and polymer science. 276, 810-815 (1998).

Yiotis, A., Boudouvis, A., Stubos, A., Tsimpanogiannis, I., Yortsos,YC: Effect of liquid films on the drying of porous media. AIChE Journal. 50, 2721-2737 (2004).

Yiotis, A., Salin, D., Tajer, E.,Yortsos, Y.: Analytical solutions of drying in porous media for gravity-stabilized fronts. Physical Review E. 85, 046308 (2012).

Yiotis, A., Salin, D., Tajer, E.,Yortsos, Y.: Drying in porous media with gravity-stabilized fronts: Experimental results. Physical Review E. 86, 026310 (2012).